Time-Resolved Infrared Studies of a Trimethylphosphine Model Derivative of [FeFe]-Hydrogenase

Melissa Johnson,[†] James Thuman,[†] Roger G. Letterman,[‡] Christopher J. Stromberg,*[,†]
Charles Edwin Webster,*[,‡] and Edwin J. Heilweil*[,§]

[†]Department of Chemistry and Physics, Hood College, 401 Rosemont Avenue, Frederick, Maryland 21701-8524 United States

[‡]Department of Chemistry, The University of Memphis, 213 Smith Chemistry Building, Memphis, Tennessee 38152-3550, United States

[§]Radiation Physics Division, Physical Measurement Laboratory, National Institute of Standards and Technology, 100 Bureau Drive, Gaithersburg, Maryland 20899-8443, United States

S *Supporting Information*

ABSTRACT: Model compounds that structurally mimic the hydrogen-producing active site of [FeFe]-hydrogenases have been studied to explore potential ground-state electronic structure effects on reaction mechanisms compared to hexacarbonyl derivatives. The time-dependent behavior of $Fe_2(\mu\text{-}S_2C_3H_6)(CO)_4(PMe)_2$ (**A**) in room temperature *n*-heptane and acetonitrile solutions was examined using various ultrafast UV and visible excitation pulses with broadband IR-probe spectroscopy of the carbonyl (CO) stretching region. Ground- and excited-state electronic and CO-stretching mode vibrational properties of the possible isomers of **A** were also examined using density functional theory (DFT) computations. In *n*-heptane, 355 and 532 nm excitation resulted in short-lived (135 ± 74 ps) bands assigned to excited-state, CO-loss photoproducts. These bands decay away, forming new long-lived absorptions that are likely a mixture of isomers of both three-CO and four-CO ground-state isomers. These new bands grow in with a time scale of 214 ± 119 ps and persist for more than 100 ns. In acetonitrile, similar results are seen with a 532 nm pump, but the 355 nm data lack evidence of the longer-lived bands. In either solvent, the 266 nm pump data seem to also lack longer-lived bands, but the intensities are significantly lower in this data, making firm conclusions more difficult. We suggest that these wavelength-dependent excitation dynamics significantly alter potential mechanisms and efficiencies for light-driven catalysis.
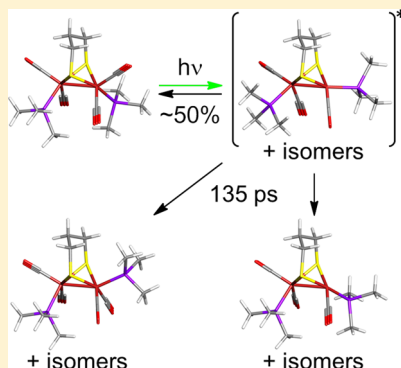
INTRODUCTION

Several microorganisms found in nature make use of enzymes known as hydrogenases to catalyze the reduction and oxidation of hydrogen, converting it between H^+ ions and H_2 molecules. [FeFe]-hydrogenases have a di-iron complex in the active site and specifically catalyze the reduction of acidic protons to hydrogen gas. The active site of [FeFe]-hydrogenase includes a combination of carbonyl (CO) and cyano (CN) ligands and a disulfur bridge (see Figure 1a).[1−7] In the past few years, studies have been conducted on model [FeFe]-hydrogenase species to improve the understanding of their structure and function. These model compounds are currently being explored as potential catalysts for the production of hydrogen and for use in fuel cells.[5−10]

There have been many attempts to synthesize complexes that are structurally related to natural hydrogenases with the hope that these model species will have efficient molecular hydrogen producing capabilities similar to the natural [FeFe]-hydrogenase.[11−27] A family of di-iron, disulfur compounds based on $Fe_2(\mu\text{-}S_2C_3H_6)(CO)_6$ have been found to structurally mimic the active site of the [FeFe]-hydrogenase enzymes.[2,4,8] Past research has paired these di-iron complexes with chromophores
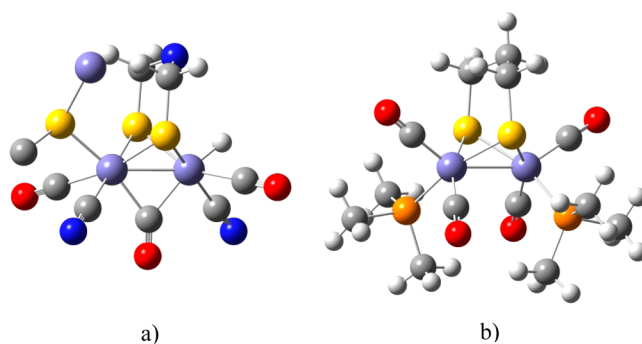

a)   b)

Figure 1. Structure of (a) the active di-iron catalytic center of the native hydrogenase and model species[1−7] compared to the (b) trans-axial/axial isomeric structure of $Fe_2(\mu\text{-}S_2C_3H_6)(CO)_4(PMe_3)_2$ (**A**, isomer **1** is shown).

that efficiently absorb solar light to drive hydrogen production, similar to the coupling of Photosystem II with a hydrogenase enzyme.[28] For this mechanism to be successful, the catalytic mechanism of the model complexes needs to occur on the same ultrafast time scale as the chromophores, that is, on the order of hundreds of picoseconds to milliseconds.[29,30] Unfortunately, very little is currently known about how the di-iron core responds to light on these time scales.

Previous studies have been conducted on $Fe_2(\mu-S_2C_3H_6)(CO)_6$ and $Fe_2(\mu-S_2C_2H_4)(CO)_6$ using ultrafast time-resolved UV and visible pump, IR probe spectroscopy (TRIR).[31−33] These studies have shown that two reaction pathways occur upon excitation with UV or visible light, with the ratio of molecules taking each pathway strongly dependent on the excitation wavelength. One of the pathways involves excitation to a short-lived ($\tau = 150 \pm 17$ ps) excited state with a longer Fe−Fe bond.[33] The second pathway involves a long-lived ($\tau = 3.7 \pm 0.26$ μs) loss of a CO ligand.[33]

The two model compounds previously studied, however, only contained CO ligands. These model compounds are not good catalysts in their own right.[34−36] The natural hydrogenases contain both CO and CN ligands,[2,5,37] while other, more effective hydrogenase model compounds have included PMe$_3$ ligands.[3,7,8,38] These ligands vary the electronic structure of the active site, thereby adjusting its catalytic properties.[3,7,8,34,36] The differences in catalytic activity raise the question of whether the time-dependent behavior of the compounds is affected by this variation. To explore this question, the ultrafast, time-dependent behavior of additional compounds with different ligands needs to be studied. An initial study of $Fe_2(\mu-S_2C_3H_6)(CO)_4(PMe_3)_2$ (**A**) has been conducted using TRIR spectroscopy with 350 nm excitation.[39] The previous work on $Fe_2(\mu-S_2C_3H_6)(CO)_6$ and $Fe_2(\mu-S_2C_2H_4)(CO)_6$ has shown the importance of using various excitation wavelengths in order to make a conclusive mechanistic analysis.[33] In the current work, $Fe_2(\mu-S_2C_3H_6)(CO)_4(PMe_3)_2$, **A**, was synthesized (Figure 1b), and its time-dependent room-temperature behavior was observed using ultrafast UV pump/ IR probe measurements of the carbonyl stretching region.

Our experiments were performed using pump wavelengths at 266 nm, 355 nm, and 532 nm, chosen to cover the UV−vis absorption spectrum (Figure 2) for this species in two different solvents: *n*-heptane and acetonitrile. In $Fe_2(\mu-S_2C_3H_6)(CO)_6$, the strong bands in the 200−400 nm region have been assigned as metal-to-ligand charge transfer bands, while the broad, weak absorption centered around 450 nm is assigned to a metal-to-

metal charge transfer band.[40] Similar assignments are expected for the UV−vis absorptions in **A**, so the bands at 270 and 344 nm are expected to be metal-to-ligand charge transfer bands, while the weak absorption centered at approximately 495 nm is expected to represent a metal-to-metal charge transfer. The compound was also modeled with DFT spectral computations. The major goal of this work was to investigate whether redistribution of electron density over the di-iron metal centers by PMe$_3$ ligand substitution affects the spectral dynamics on the IR time scale.

■ EXPERIMENTAL AND COMPUTATIONAL METHODS

Synthesis of $Fe_2(\mu-S_2C_3H_6)(CO)_6$ was first conducted according to literature methods.[8] $Fe_3(CO)_{12}$ and 1,3-propane-dithiol (all reagents were purchased from Sigma-Aldrich[41] and used as received) were combined under nitrogen atmosphere, heated to 350 K, and allowed to react for 3−5 h. After the reaction was completed, the sample was filtered and evaporated to dryness under a vacuum. It was then redissolved in hexanes, filtered, and evaporated to dryness again. Synthesis of **A** was carried out by combining $Fe_2(\mu-S_2C_3H_6)(CO)_6$ with PMe$_3$ under an argon atmosphere and refluxing overnight at 343 K. Upon completion of the reaction, the sample was filtered and evaporated to dryness.[38]

Time-Resolved UV−visible Excitation/IR Probe Laser Spectroscopy (TRIR). A Nd:Vanadate diode-pumped laser (10 ps, 2 W at 532 nm, 80 MHz) was used to synchronously pump two tunable dye lasers and seed a 20 Hz Nd:YAG regenerative amplifier.[42] The two dye lasers, one tuned to 656 nm and the other to 589 nm, were amplified by the 25 mJ/ pulse, 532 nm output of the Nd:YAG regenerative amplifier and combined to produce 150 fs tunable broadband IR pulses (ca. 80 cm^{-1} fwhm; full width at half-maximum) ranging from 1930 cm^{-1} to 2100 cm^{-1}. For these short-delay time experiments (0−700 ps), residual 1.064 μm, 60 ps fwhm pulses from the Nd:YAG amplifier were used to generate optically delayed 30 ps, 40 ps, and 50 ps excitation harmonics at 266 nm, 355 nm, and 532 nm, respectively. Typical excitation pulse energies were 50 μJ, 150 μJ, and 1 mJ per pulse at the sample (at 266 nm, 355 nm, and 532 nm, respectively). The pump and probe beam sizes were approximately 0.5 mm and 0.1 mm diameter, respectively. The estimated maximum peak pump fluence corresponds to at most 1.2 GW/cm^2 within the sample.

Excitation and probe beams were combined and focused into solutions of **A** in argon-purged *n*-heptane and acetonitrile. Typical solution concentrations were chosen so the optical densities (OD) for both pump and probe static absorption feature wavelengths were less than OD = 1 when flowed through a 2 mm path length cell fitted with CaF$_2$ windows. Half of the generated IR probe beam was sent through a separate part of the solution to provide a spectral reference signal. The IR signal and reference beams were sent through a monochromator and onto a 256 × 256 pixel InSb focal plane detector for spectral analysis (ca. 4 cm^{-1} fwhm spectral resolution). Up to five independent scans of 2000 laser shots, taking approximately 4−6 min each, were averaged to produce transient difference spectra at specified excitation-probe time delays. Error estimates for transient spectral feature lifetimes are reported as simple standard deviations from the mean for a single exponential fit ($k = 1$ analysis). Under all excitation wavelengths and pulse durations, measured difference spectral
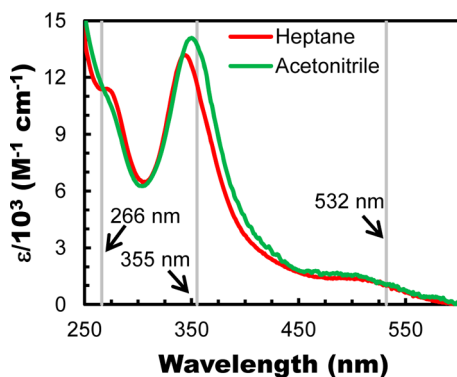

Figure 2. UV−visible absorption spectra of **A** dissolved in *n*-heptane (green) and acetonitrile (red) at room temperature.

15793

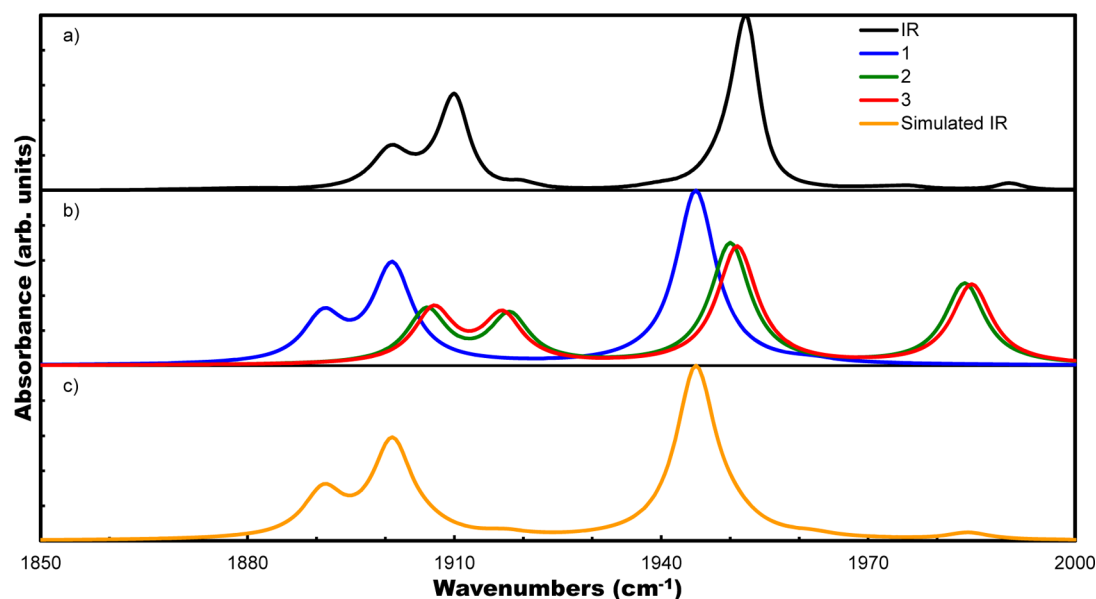dx.doi.org/10.1021/jp4067873 | J. Phys. Chem. B 2013, 117, 15792−15803

Figure 3. (a) Experimental IR spectrum of **A** in *n*-heptane. (b) Simulated IR spectra (BVP86/BS2) of isomers **1** (blue), **2** (green), and **3** (red). (c) Simulated IR spectrum of **A** using 92% **1**, 4% **2**, and 4% **3**. All Lorentzian functions have a width of 7 cm^{-1} in the simulated spectra.
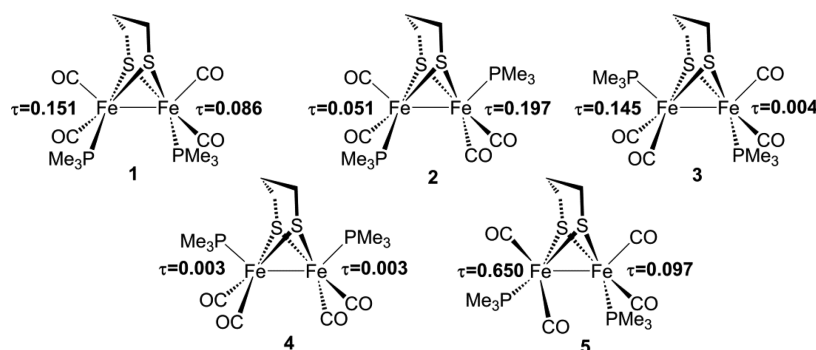

Figure 4. Structural diagrams of the optimized ground-state complexes with τ values indicated. Isomers are labeled from lowest to highest energy. The τ values shown in the figure are a measure of the geometry around the iron (assuming a five-coordinate geometry and ignoring the Fe−Fe bond). A τ value of 0 is a perfectly square pyramidal geometry, while a τ value of 1 is perfectly trigonal bipyramidal.[68]

intensities were found to be linear with excitation pulse fluence at a given delay time.

Computational Details. Theoretical calculations for ground state isomeric structures of **A** were carried out using the Gaussian 03W[43] implementation of the BP86[44−46] density functional theory (DFT)[47] using default grids, default convergence criteria, and the TZVP basis sets for all atoms (basis set 1, BS1).[48,49] The initial structure for the geometry optimization of compound **A** was taken from the crystallographic data of Fe$_2(\mu$-S$_2$C$_3$H$_6$)(CO)$_6$ (CCDC No. 127014).[50] Theoretical calculations were also carried out using the Gaussian 09[51] implementation of BVP86 (the B[44] exchange functional and the VP86 correlation functional[45,46,52,53]) density functional theory (DFT),[47] using the default pruned fine grids for energies (75, 302), default pruned course grids for gradients and Hessians (35, 110) (neither grid is pruned for iron), and nondefault SCF convergence for geometry optimizations (10^{-6}). In basis set 2 (BS2), the basis set for iron (341/341/41) was the Hay and Wadt basis set and effective core potential (ECP) combination (LANL2DZ)[54] as modified by Couty and Hall,[55] where the two outermost p functions have been replaced by a (41) split of the optimized chromium 4p function. The 6-31G(d)[56,57] basis set was used

for hydrogen, phosphorus, and sulfur atoms, and the 6-31G(d′)[56−58] basis set was used for all other atoms. The density fitting approximation[59−62] for the fitting of the Coulomb potential was used for all BVP86/BS2 computations; auxiliary density-fitting basis functions were generated automatically (by the procedure implemented in Gaussian 09) for the specified AO basis set. Spherical harmonic d functions were used throughout; that is, there are five angular basis functions per d function. Excited-state structures were geometry optimized with BVP86/BS2 employing time-dependent density functional theory (TDDFT)[63] using analytical gradients.[64,65] All structures were fully optimized. Analytical frequency calculations were performed on all ground-state DFT structures, and numerical frequency calculations were performed on all TDDFT excited-state structures to ensure either a zeroth-order saddle point (a local minimum) or a first-order saddle point (transition state: TS) was achieved.[66] All energies, enthalpies, and Gibbs free energies reported have been calculated using standard conditions (298.15 K and 1 atm). All reported IR frequencies were scaled in the same manner as those reported in a previous publication.[33] The simulated IR spectra were produced with an in-house program using Lorentzian broadening (7 cm^{-1} for simulations in *n*-heptane

Table 1. Select Parameters of Ground State Coordinatively Saturated Species, Calculated Using BVP86/BS2

	ΔG (kcal mol^{-1})^a	Fe—Fe distance(Å)	ω_{harm} (cm^{-1})^b	int (km/ mol)	ω_{harm} (cm^{-1})^b	int (km/ mol)	ω_{harm} (cm^{-1})^b	int (km/ mol)	ω_{harm} (cm^{-1})^b	int (km/ mol)
1	0.00	2.569	1885	367	1895	779	1939	1387	1956	24
2	0.42	2.525	1900	427	1912	384	1944	964	1978	646
3	0.50	2.526	1902	431	1912	380	1945	938	1979	637
4	2.14	2.493	1917	2	1941	938	1951	393	1998	1008
5	3.35	2.600	1892	258	1915	530	1934	1150	1972	606

$^a\Delta G$ is relative to **1**, the most stable isomer. ^{b}Gas phase scaled-harmonic frequencies.

and 14 cm^{-1} in acetonitrile). Simulated UV−vis spectra were also produced with an in-house program using Gaussian broadening (30 nm).

Efforts to optimize **1-3***, **2-4***, **3-1***, **3-2***, **4***, **4-4***, and **5-1*** were unsuccessful.[67] In each case, the error was encountered in Link 801 during the initialization of the transformation to two-electron integrals.

■ RESULTS AND DISCUSSION

FTIR of A in *n*-Heptane Solution. The ground state FTIR spectrum of **A** in *n*-heptane solution at room temperature has three major CO-stretching band absorptions in the mid-infrared region at 1900 cm^{-1}, 1910 cm^{-1}, and 1952 cm^{-1}, as shown in Figure 3a. Much weaker absorptions are found at 1920 cm^{-1} and 1990 cm^{-1}.

There are five isomers possible for **A** (not counting enantiomers), as shown in Figure 4. The τ values shown in the figure are a measure of the geometry around the iron (assuming a five-coordinate geometry and ignoring the Fe—Fe bond). A τ value of 0 is a perfectly square pyramidal geometry, while a τ value of 1 is perfectly trigonal bipyramidal.[68]

DFT computations were performed on each isomer, with the results for BS2 shown in Table 1 (results from BS1 are provided in the Supporting Information; see Tables S1 and S2). Of the five isomers, only isomer **1** matches the predominant bands of **A** in *n*-heptane. This isomer has both of the PMe$_3$ ligands in axial positions, trans to each other, in agreement with previous results[39] and the crystal structure of **A**.[38]

The minor bands at 1920 cm^{-1} and 1990 cm^{-1} most likely come from additional isomers of **A**, in particular **2** and **3** (spectra shown in Figure 3b). While a spectrum created assuming a Boltzmann distribution population between the isomers (using the gas-phase ΔG values shown in Table 1) does not fit the experimental spectrum well, a simulated spectrum assuming 92% **1**, 4% **2**, and 4% **3** (shown in Figure 3c) better matches the experimental spectrum.

The low amount of isomers **2** and **3** compared to what is expected from the Boltzmann distribution is likely due to polarity differences between the isomers. Using BVP86/BS2, the dipole moments are computed to be 2.046, 4.694, and 4.879 D for isomers **1**, **2**, and **3**, respectively. Since *n*-heptane is nonpolar, the less polar isomer would be expected to be more stable, while the more polar isomers would be less stable, shifting the distribution of isomers away from what would be expected based solely on the computed energies (assuming that those energies are exact). This result is consistent with the results found in ref 39.

TRIR of A in *n*-Heptane Solution. Differential time-resolved TRIR spectra of **A** in room temperature *n*-heptane solution are shown in Figure 5 from 1850 cm^{-1} to 2000 cm^{-1} for the three different UV and visible-excitation wavelengths at various delay times relative to excitation. In the time-resolved
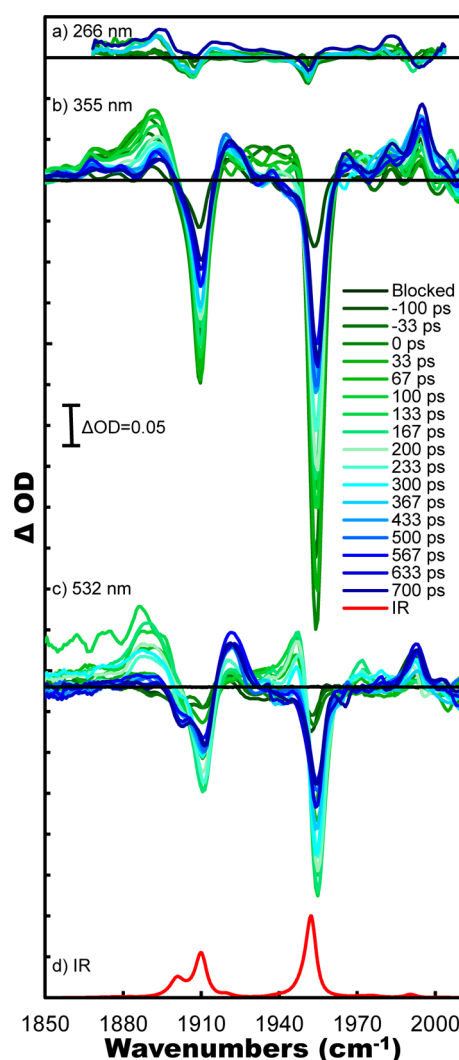

Figure 5. UV and visible pump, IR probe differential transient spectra for **A** in room temperature *n*-heptane using (a) 266 nm, 30 ps fwhm, (b) 355 nm, 40 ps fwhm, and (c) 532 nm, 50 ps fwhm excitation pulses. (d) FTIR spectrum of ground state **A** in *n*-heptane.

differential spectra, the strong absorptions, corresponding to isomer **1**, appear as bleaching features (negative OD), implying that a fraction of the original compound has been lost after excitation.

Two types of photoproducts appear as new absorptions in the data. The first set of new absorption bands is observed at 1893 cm^{-1}, 1947 cm^{-1}, and 1972 cm^{-1} in the 355 and 532 nm excitation data. These bands are readily observed, primarily in the green spectra (early and intermediate delay times) in Figure 5b for 355 nm excitation. They are even more distinct in the 532 nm excitation data shown in Figure 5c. These bands grow

in rapidly and decay with a time constant of 135 ± 74 ps (peak kinetics depicted in Figure 6). All time-decays are derived from both the 355 and 532 nm data, as the spectral dynamics are similar for both pump wavelengths.
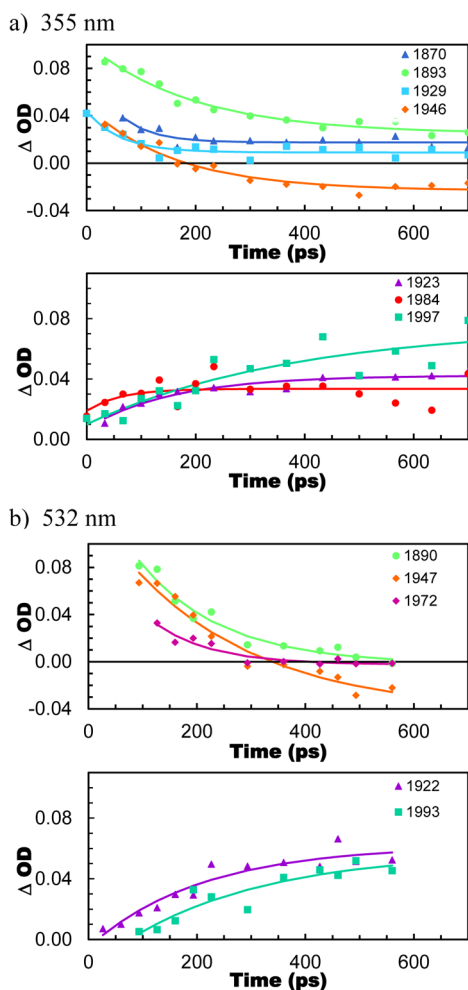

Figure 6. Time dependence at selected IR wavelengths (cm^{-1}) for **1** in *n*-heptane at 293 K. Top plots display wavelengths corresponding to decay of the short-lived species; bottom plots display wavelengths corresponding to the longer-lived species when using (a) 355 nm excitation, (b) 532 nm excitation.

A second set of bands grows in with a time constant of 214 ± 119 ps, as the short-lived bands are decaying away, implying that the shorter-lived photoproduct is converting into the longer-lived species (see Figure 6). These bands are shown in the blue spectra (later delay times) in Figure 5b and are observed at 1895 cm^{-1}, 1922 cm^{-1}, and 1995 cm^{-1}. These long-lived bands persist out to at least 200 ns (data not shown). The same bands are observed in the 532 nm excitation data shown in Figure 5c. There is some overlap between the two types of bands throughout the data, as seen at 1926 cm^{-1} in both the 355 and 532 nm excitation data.

The data for the 266 nm excitation are significantly lower in intensity, making interpretation much more difficult. Distinct differences are seen between the 266 nm data and the 355 and 532 nm results. The 266 nm data show only a single, long-lived set of bands, but these long-lived bands seem to have characteristics of both the short- and long-lived bands seen in

the 355 and 532 nm data. The low signal-to-noise-ratio makes further conclusions about the 266 nm data speculative, at best.

The strongly reduced transient bleach and absorption intensities observed in the 266 nm TRIR data may be a combined result of lower quantum yields, fewer available pump photons, and interference from PMe_3 ligand absorption that interferes with CO photodissociation through typical metal-charge transfer absorption. Estimates for expected bleach signal levels using the measured sample absorption at 266 nm, available number of pump photons, and a 2-fold increased absorption by PMe_3 at 266 nm compared to the $Fe_2(\mu\text{-}S_2C_3H_6)(CO)_6$ analogue suggested these signals should be reduced by only a factor of 3−4, which is not observed when compared to the 355 and 532 nm data. This result was consistent over many experimental runs and conditions, suggesting an inefficient dissociative mechanism or lower quantum yield because of the PMe_3 ligand-modified electronic structure. This hypothesis requires further scrutiny.

For newly formed product species with similar absorption cross sections as the reactant, bleach features are generally found to extend below the zero-differential baseline, which is the case for **A** when using 266 nm, 355 nm, and 532 nm excitation. Previous work with $Fe_2(\mu\text{-}S_2C_3H_6)(CO)_6$ showed strong, short-lived product absorptions, particularly when excited with 532 nm light, with these new absorptions overwhelming some of the bleaching features. No such strong product absorptions were observed in this work at any pump wavelength, implying that the electronic properties of **A** are quite different from the all-CO version of the compound. This result is reinforced by the DFT-calculated Mulliken charges, shown in Table S3, Supporting Information. The electron density on the Fe atoms is significantly larger for all five isomers of **A** than those for $Fe_2(\mu\text{-}S_2C_3H_6)(CO)_6$. Values for selected CO-loss isomers and excited state species are shown in Tables S3 and S4, Supporting Information.

Similar differential mid-infrared absorption spectra have been previously published for **A** over picosecond to nanosecond time delays using only 350 nm excitation wavelength.[39] Spectra presented in that paper and in this work exhibit strong below baseline bleaches resulting from loss of the original compound and weaker product absorption features. Minor discrepancies between previously published spectra compared to those in Figure 5b obtained with 355 nm excitation most likely results from differences in excitation fluence or the initial concentration of **A**.[33] Overall, the observed time-dependent spectral features from both studies agree rather well when using 350 or 355 nm excitation wavelengths.

In order to help explain the new absorption features seen in the TRIR data of **A**, DFT computations were performed to predict the vibrational energies of all of the possible CO loss fragments of **A** using both BS1 and BS2. The results for ground-state BS2 calculations are shown in Figure 7 and Table 2 (similar results for BS1 are included in the Supporting Information). Results for BS2 calculations on excited state, coordinatively saturated species are shown in Table 3, while results for excited state CO-loss products are shown in Table 4. Figures summarizing these results are included in the Supporting Information as Figures S1 and S2.

Potential PMe_3 loss fragments were also calculated using BS1, but these spectra had all vibrational modes shifted significantly higher in wavenumber than the corresponding vibrational modes of **1**, making them poor matches for either the short- or long-time photofragments (data not shown).
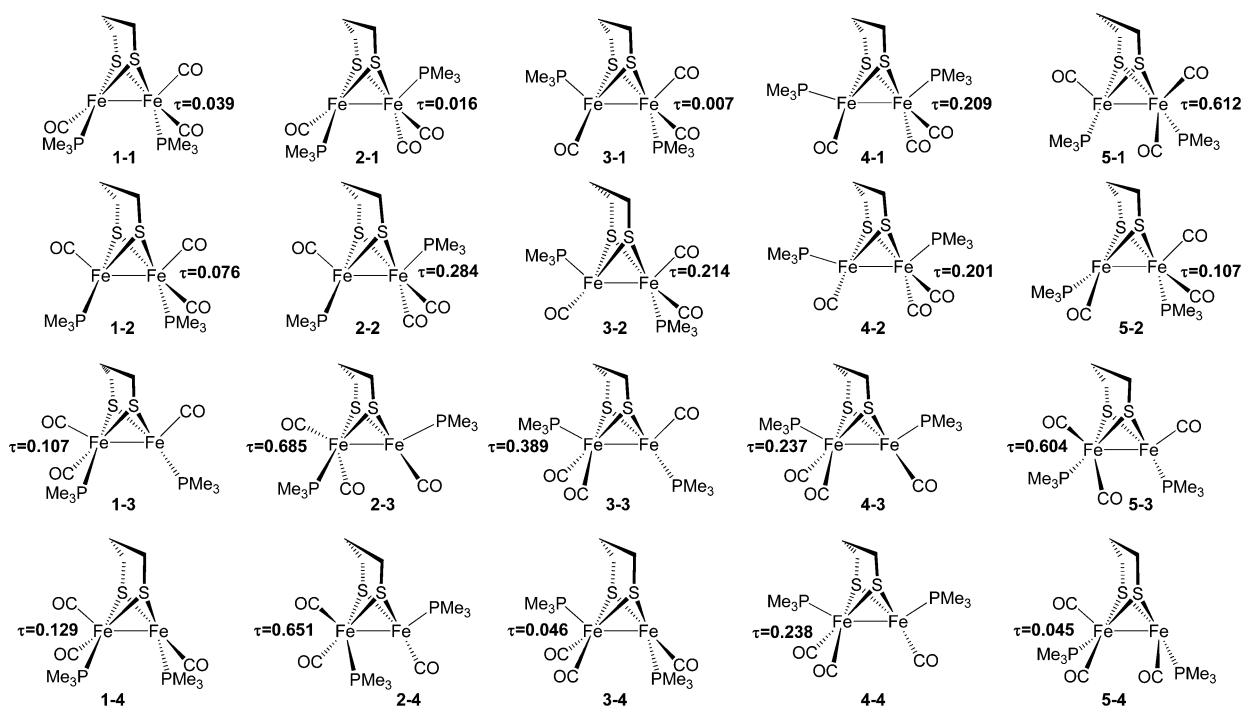
Figure 7. Structural diagrams of the optimized ground-state one CO-loss products with τ values indicated.

Table 2. Select Parameters of Ground State One CO-Loss Products, Calculated Using BVP86/BS2

	ΔG (kcal mol^{-1})^a	Fe–Fe distance (Å)	ω_{harm} (cm^{-1})^b	int (km/mol)	ω_{harm} (cm^{-1})^b	int (km/mol)	ω_{harm} (cm^{-1})^b	int (km/mol)
3-3	37.41	2.506	1891	998	1894	450	1942	502
1-3	38.71	2.568	1882	945	1894	597	1940	649
2-3	38.91	2.494	1879	181	1892	1266	1931	629
1-2	39.16	2.571	1884	1009	1891	581	1939	627
2-4	39.65	2.469	1892	448	1919	805	1967	941
3-1	40.03	2.505	1889	187	1911	1063	1959	862
5-3	40.25	2.532	1836	531	1890	1177	1913	433
2-2	40.26	2.504	1891	1055	1894	423	1943	522
4-3	40.61	2.466	1899	478	1920	534	1971	930
1-1	41.99	2.512	1858	714	1901	593	1954	560
3-2	42.26	2.516	1871	600	1902	765	1945	720
1-4	42.63	2.514	1857	721	1899	604	1951	557
2-1	42.90	2.474	1891	614	1908	508	1971	681
4-1	42.98	2.466	1901	452	1919	544	1971	957
5-1	44.33	2.564	1879	644	1892	1073	1926	487
3-4	44.34	2.481	1889	641	1908	487	1972	672
5-2	44.48	2.538	1885	321	1914	893	1967	722
5-4	45.59	2.544	1882	377	1913	856	1967	743

$^a\Delta G$ is relative to **1** (calculated as the difference of products minus reactants for CO loss). ^{b}Gas phase scaled-harmonic frequencies.

Table 3. Select Parameters of First Excited State Coordinatively Saturated Species, Calculated Using BVP86/BS2

	ΔG (kcal mol^{-1})^a	Fe–Fe distance (Å)	ω_{harm} (cm^{-1})^b	int (km/mol)	ω_{harm} (cm^{-1})^b	int (km/mol)	ω_{harm} (cm^{-1})^b	int (km/mol)	ω_{harm} (cm^{-1})^b	int (km/mol)
1*	34.93	2.883	1855	289	1891	760	1938	112	1976	335
2*	37.65	2.862	1887	571	1918	221	1951	937	1981	504
3*	38.71	2.777	1880	301	1911	478	1973	158	1986	614
5*	38.46	2.881	1884	636	1898	294	1951	907	1982	284

$^a\Delta G$ is relative to **1**, the most stable ground state isomer. ^{b}Gas phase scaled-harmonic frequencies.

Comparing the short-lived bands at 1893 cm^{-1}, 1947 cm^{-1}, and 1972 cm^{-1} to the BS2 results, the only single isomer whose peak wavenumbers match these bands is the excited state, CO-loss isomer **1-4*** (see Table 4). Since the vast majority of **A** in

n-heptane is in the form of isomer **1**, forming a CO-loss product directly from this isomer is logical. Unfortunately, simulated difference spectrum assuming that **1-4*** is the only photoproduct affords intensities that do not match well with

Table 4. Select Parameters of First Excited State One CO-loss Products, Calculated Using BVP86/BS2

	ΔG (kcal mol^{-1})^a	Fe–Fe distance (Å)	ω_{harm} (cm^{-1})^b	int (km/mol)	ω_{harm} (cm^{-1})^b	int (km/mol)	ω_{harm} (cm^{-1})^b	int (km/mol)
1-1*	54.69	2.519	1873	480	1900	737	1954	659
1-4*	55.02	2.511	1883	183	1926	426	1948	403
5-2*	55.34	2.493	1886	70	1909	1016	1967	804
3-3*	56.24	2.470	1888	766	1898	468	1956	558
2-1*	57.05	2.467	1908	439	1923	559	1986	756
5-3*	58.13	2.487	1841	665	1891	1047	1919	465
2-2*	58.94	2.472	1883	882	1894	435	1954	562
1-2*	59.56	2.513	1858	717	1887	871	1927	581

$^a\Delta G$ is relative to **1** (calculated as the difference of products minus reactants for CO loss). ^{b}Gas phase scaled-harmonic frequencies.

the experimental data (see Figure 8b). By adding in equal amounts of excited state CO-loss products **1-1***, **1-2***, **1-4***, **2-**
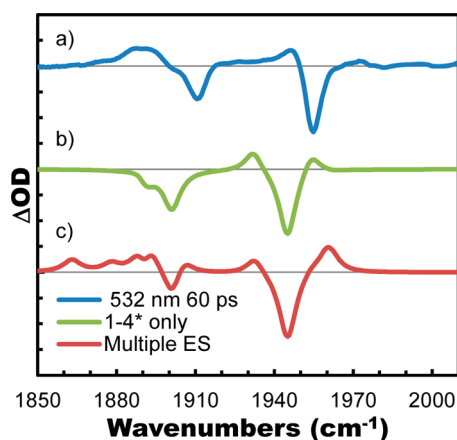

Figure 8. (a) Experimental difference spectrum with 532 nm pump at 60 ps. (b) Simulated difference spectrum using **1-4*** excited state CO-loss product only. (c) Simulated difference spectrum using equal amounts of **1-1***, **1-2***, **1-4***, **2-2***, and **3-3*** excited state CO-loss products.

2*, and **3-3***, a better, though still not perfect, match can be obtained (see Figure 8c). Given the large number of possible isomers, an exact fit obtained from varying the amount of various isomers is not practical. The spectrum in Figure 8c with all isomers equally represented is shown for justification purposes only. Addition of some derivatives of isomers **2** and **3** seems to be required in order to get the bands near 1893 cm^{-1} to be intense enough compared to the other bands. This analysis is limited in part because results from all of the excited state CO-loss isomers were not obtainable. However, not all isomers can be included and still obtain a good match to the experimental spectrum (for instance, including **2-1*** results in a band at 1992 cm^{-1}, which is not present in the experimental data).

The assignment of the short-time species as a CO loss product is consistent with previous work;[39] however, the previous study and analysis did not address the question of which isomer was generated in the photofragmentation process, and excited-state isomers were not considered.

As time progresses, the excited state molecules decay. Roughly 50% of the initial short-time photoproduct appears to convert back to **1** through geminate recombination, as seen by the partial recovery of all strong three bleach features, seen in Figure 5b,c. The remaining 50% convert to secondary photoproducts.

There are two possibilities here. The first is that the molecules recombine with CO as they decay, returning to a coordinatively saturated species. Since a long-time difference frequency spectrum is observed, the molecules would have to have interconverted into a different isomer. This mechanism is proposed in the previous work.[39] A comparison of the experimental difference spectrum (with 355 nm pump at 700 ps) with two different simulated spectra comprised of coordinatively saturated species is shown in Figure 9 (isomer
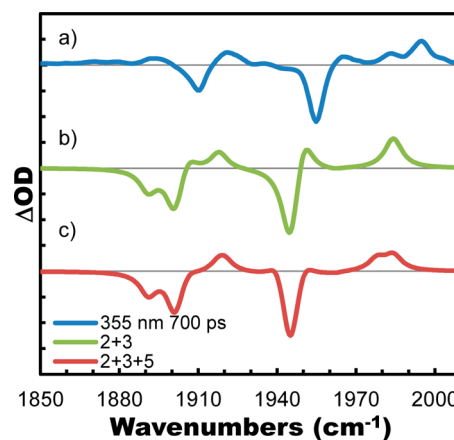

Figure 9. (a) Experimental difference spectrum with 355 nm pump at 700 ps. (b) Simulated difference spectrum using **2** and **3** ground state, coordinatively saturated isomers. (c) Simulated difference spectrum using **2**, **3**, and **5** ground state, coordinatively saturated isomers.

4 is not included in either simulated spectrum, as it includes a very high wavenumber band not seen in the experimental data). Both possibilities fit the experimental spectrum quite well above 1900 cm^{-1}; however, neither possibility shows any new absorption below 1900 cm^{-1}, as is seen in the 355 nm data. Thus, a purely ground state, coordinatively saturated combination is unlikely, especially for the 355 nm data (the 532 nm data fit this explanation somewhat better, as the band around 1895 cm^{-1} is either significantly less pronounced or absent from the long-time data).

Another possibility is that the excited state decays to a coordinatively unsaturated photoproduct. As with the short-time results, there is a single isomer (**3-4**) that seems to fit the new absorptions reasonably well (Figure 10b), but a combination of multiple isomers (for instance, the combination of **1-1**, **1-2**, **1-3**, **1-4**, **2-1**, **2-2**, **2-3**, **2-4**, **3-1**, **3-2**, **3-3**, and **3-4** shown in Figure 10c) is perhaps more realistic. These two possibilities are not mutually exclusive, and a combination of both saturated and unsaturated secondary photoproducts is likely present.
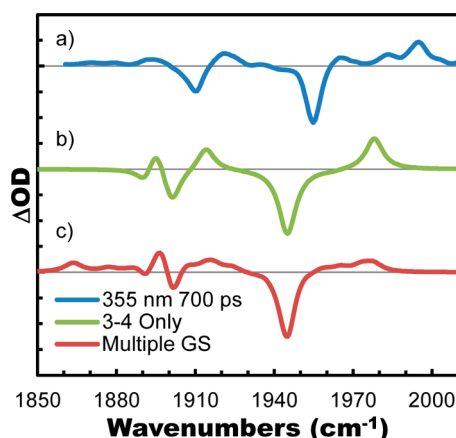
Figure 10. (a) Experimental difference spectrum with 355 nm pump at 700 ps. (b) Simulated difference spectrum using **3-4** ground state, coordinatively unsaturated isomer. (c) Simulated difference spectrum using **1-1**, **1-2**, **1-3**, **1-4**, **2-1**, **2-2**, **2-3**, **2-4**, **3-1**, **3-2**, **3-3**, and **3-4** ground state, coordinatively saturated isomers.

FTIR of A in Acetonitrile Solution. The infrared bands of **A** in acetonitrile solution are significantly broader than those in *n*-heptane, as can be seen in Figure 11a. The same isomers (**1**, **2**, and **3**) can be used to model this spectrum, but the proportions of the isomers are significantly different. The spectrum in Figure 11c was generated using 60% isomer **1**, 20% isomer **2**, and 20% isomer **3**. The simulated bands are wider than those in Figure 3 (14 cm^{-1} versus 7 cm^{-1}). Note that these percentages are very close to those that would be generated assuming a Boltzmann distribution of the three isomers (for a Boltzmann distribution, the percentages would be 52%, 26%, and 22%).

The reason for the significantly higher proportions of isomers **2** and **3** in acetonitrile can be explained by the computed dipole moments of the isomers. As mentioned above, the BVP86/BS2 computed dipole moments for **1**, **2**, and **3** are 2.046, 4.694, and

4.879 D, respectively (the calculated dipole moments of additional species are reported in the Supporting Information). The more polar isomers should be more stable in a polar solvent, giving rise to the increased amounts of isomers **2** and **3** in acetonitrile versus *n*-heptane.

TRIR of A in Acetonitrile Solution. The time-resolved differential absorption spectra for **A** in room temperature acetonitrile using the three pump wavelengths are shown in Figure 12. The corresponding kinetic plots for 355 and 532 nm are shown in Figure 13. The broad IR absorptions for the unexcited molecule, shown in Figure 12d, again generate bleach features in the time-resolved spectra of Figure 12a–c.

The 532 nm data for **A** in acetonitrile (Figure 12c) are very similar to that for **A** in *n*-heptane, with the exception of broader bands resulting from the more polar solvent. The short-time 355 nm data are similar to the 532 nm short-time data in acetonitrile; however, the long-time data are somewhat different, as there is little to no evidence of the longer-lived isomer shown in Figures 5b,c and 12c. There is, however, evidence that some of the initial photoproduct survives for very long times (out to 15 μs, data not shown). This behavior is consistent with the 266 nm data obtained in both solvents (Figures 5a and 12a).

On first inspection, the reason for a pump-wavelength dependence of the long-time data is not entirely obvious. One possible explanation for this result is that there are differences in the UV−vis absorption of the different isomers. The simulated UV−vis spectrum for **1**, **2**, and **3** are shown in the Supporting Information, Figure S3. The comparison of these spectra demonstrates the differences of the computed oscillator strengths at higher versus lower wavelengths. The wavelength dependence of the experimental spectra may be due, in part, to the stronger absorption of higher energy photons in **2** and **3** versus **1** at shorter wavelengths, indicating that a more significant quantity of **2** and **3** may undergo photolysis compared to **1**. This effect would be stronger in acetonitrile, as more of **2** and **3** exist in an acetonitrile solution.
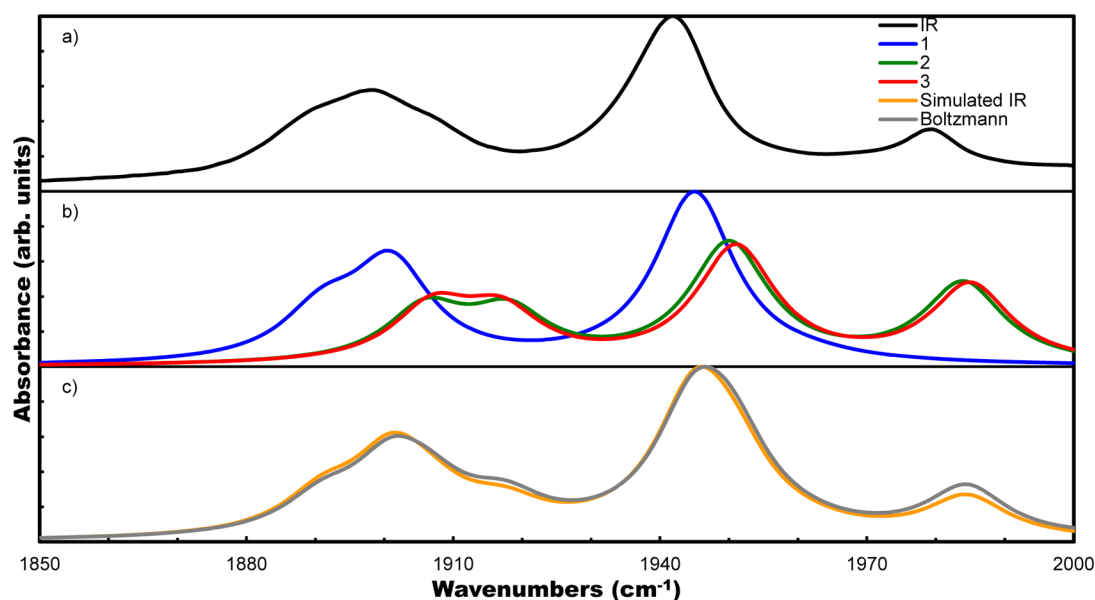

Figure 11. (a) Experimental IR spectrum of **A** in acetonitrile. (b) Simulated IR spectrum (BVP86/BS2) of isomers **1** (blue), **2** (green), and **3** (red). (c) Simulated IR spectrum of **A** using 60% **1**, 20% **2**, and 20% **3**. Also shown (in gray) is a simulated IR spectrum assuming a Boltzmann distribution of isomers **1−3**. All Lorentzian functions have a width of 14 cm^{-1} in the simulated spectra.
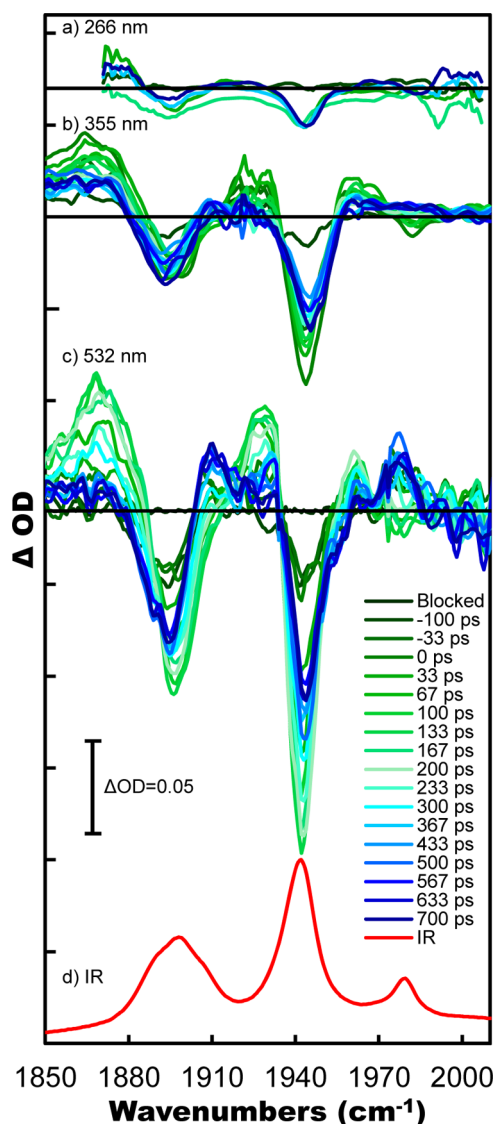
Figure 12. UV and visible pump, IR probe differential transient spectra for **A** in room temperature acetonitrile using (a) 266 nm, 30 ps fwhm, (b) 355 nm, 40 ps fwhm, and (c) 532 nm, 50 ps fwhm excitation pulses. (d) FTIR spectrum of ground state **A** in acetonitrile.
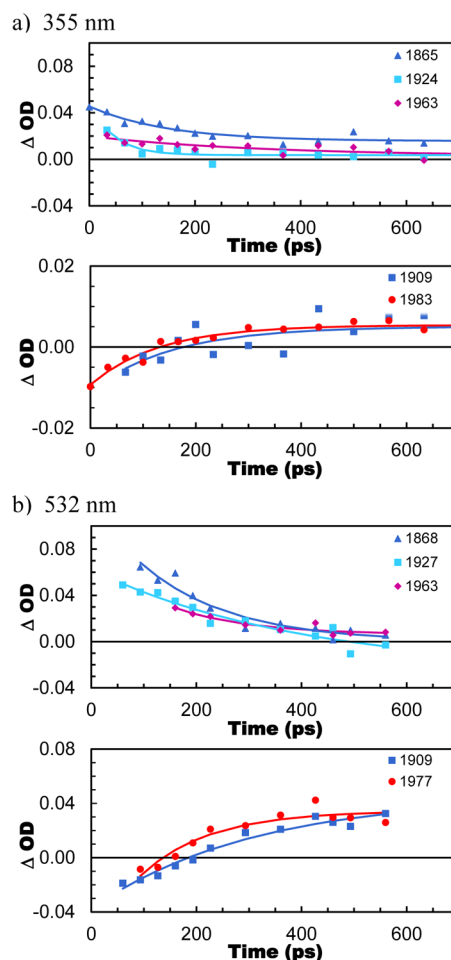

Figure 13. Time dependence of peak absorption features of **A** in room temperature acetonitrile at indicated IR wavelengths (cm^{-1}). Top plots display wavelengths corresponding to the short-lived species (green in Figure 12); bottom plots display wavelengths corresponding to the long-lived species (blue in Figure 12) using (a) 355 nm and (b) 532 nm excitation.

CONCLUSIONS AND FUTURE PROSPECTS

In *n*-heptane solution, **A** exists primarily as isomer **1**, with small amounts of **2** and **3** present. Upon UV or visible excitation, **A** in *n*-heptane undergoes loss of a CO ligand, resulting in a complicated mixture of three-CO, excited state isomers. These excited states then relax to a mixture of ground state isomers. For some of the molecules, the relaxation appears to involve recombination with CO, resulting in a higher proportion of isomers **2** and **3**, but not all of the molecules undergo this recombination. A similar sequence appears to be followed when **A** is dissolved in acetonitrile. Substantial pump-wavelength dependent differences in the isomers generated are seen, however, especially in acetonitrile. The wavelength dependence likely arises from the difference in the electronic absorption coefficients for the different isomers. A greater effect is seen in acetonitrile because a greater proportion of the more polar isomers **2** and **3** are present in this more polar solvent.

This behavior is significantly different than the behavior observed previously with $Fe_2(\mu\text{-}S_2C_3H_6)(CO)_6$.[33] In $Fe_2(\mu\text{-}$

$S_2C_3H_6)(CO)_6$, a short-lived, coordinatively saturated excited state species was observed that is not formed with **A**. Also, because $Fe_2(\mu\text{-}S_2C_3H_6)(CO)_6$ only contains CO ligands, issues related to isomerization are greatly reduced. These differences show the significant impact of varying the ligands (and thus the electronic structure of the active site) on the dynamic behavior.

When considering the proposed light-driven catalytic mechanisms similar to photosystem II coupled to a hydrogenase enzyme, those designing such catalysts must be aware that the active site may be affected by the wavelength of light used to drive the reaction and the electronic structure of the Fe centers in the active site induced by pendant ligands. The dynamic behavior of the active site has the potential to drastically affect the success of the mechanism. The loss of a CO ligand, for instance, provides an unoccupied site that has the possibility of being either beneficial or detrimental to hydrogen producing mechanisms.

Future research will include studying the ethyl bridge variant of **1** at all three wavelengths. The study of the entire series of model compounds $[Fe_2(\mu\text{-}S_2R)(CO)_{6-n}(CN)_n]^{n-}$, where the R group is either propyl or ethyl and *n* ranges from 0 to 2 is also of further interest. The CN ligands in these molecules have a higher similarity to the true catalytic site of the [FeFe]-

15800

dx.doi.org/10.1021/jp4067873 | *J. Phys. Chem. B* 2013, 117, 15792−15803

hydrogenase enzyme, and the addition of CN may yield additional potential photofragments, including the loss of CN from the active site. Ideally, these experiments will involve exciting each compound at all three wavelengths and probing the dynamics from 50 ps out to at least 15 μs. Although the photodissociation of metal carbonyls has been studied extensively, much less work has been performed on the metal cyanide derivatives.

■ ASSOCIATED CONTENT

Ⓢ Supporting Information

Further details of computational results are available, including full citation for refs 43 and 51. This material is available free of charge via the Internet at http://pubs.acs.org.

■ AUTHOR INFORMATION

Corresponding Authors

*(C.J.S.) E-mail: stromberg@hood.edu. Phone: (301) 696-3678. Fax: (301) 696-3667.
*(C.E.W.) E-mail: cewebstr@memphis.edu. Phone: (901) 678-3293. Fax: (901) 678-3447.
*(E.J.H.) E-mail: edwin.heilwil@nist.gov. Phone: (301) 975-2370. Fax: (301) 975-5524.

Notes

The authors declare no competing financial interest.

■ REFERENCES

(1) Bennett, B.; Lemon, B. J.; Peters, J. W. Reversible Cabon Monoxide Binding and Inhibition at the Active Site of the Fe-Only Hydrogenase. *Biochemistry* **2000**, *39*, 7455.

(2) Popescu, C. V.; Eckard, M. Electronic Structure of the H cluster in [Fe]-Hydrogenases. *J. Am. Chem. Soc.* **1999**, *121*, 7877.

(3) van der Vlugt, J. I.; Rauchfuss, T. B.; Wilson, S. R. Electron-Rich Diferrous-Phospane-Thiolates Relevant to Fe-only Hydrogenase: Is Cyanide "Nature's Trimethylphospane"? *Chem.—Eur. J.* **2006**, *12*, 90.

(4) Wang, X.-B.; Niu, S.; Yang, X.; Ibrahim, S. K.; Pickett, C. J.; Ichiye, T.; Wang, L.-S. Probing the Intrinsic Electronic Structure of the Cubane [4Fe-4S] CLuster, Nature's Favorite Cluster for Electron Transfer and Storage. *J. Am. Chem. Soc.* **2003**, *125*, 14072.

(5) Adams, M. W.; Stiefel, E. L. Organomettalic iron: the key to biological hydrogen meabolism. *Chem. Biol.* **2000**, *4*, 214.

(6) Nicolet, Y.; Lemon, B. J.; Fontecilla-Camps, J. C.; Peters, J. W. A novel FeS cluster in Fe-only hydrogenases. *Trends Biochem. Sci.* **2000**, *25*, 138.

(7) Gloaguen, F.; Lawrence, J. D.; Rauchfuss, T. B. Biomimetic Hydrogen Evolution Catalyzed by an Iron Carbonyl Thiolate. *J. Am. Chem. Soc.* **2001**, *123*, 9476.

(8) Gloaguen, F.; Lawrence, J. D.; Schmidt, M.; Wilson, S. R.; Rauchfuss, T. B. Synthetic and Structural Studies on $[Fe_2(SR)_2(CN)_x(CO)_{6-x}]^{x-}$ as Active Site Models for Fe-Only Hydrogenases. *J. Am. Chem. Soc.* **2001**, *123*, 12518.

(9) Lyon, E. J.; Georgakaki, I. P.; Reibenspies, J. H.; Darensbourg, M. Y. Coordination Sphere Flexibility of Active-Site Models for Fe-Only Hydrogenase: Studies in Intra- and Intermolecular Diatomic Ligand Exchange. *J. Am. Chem. Soc.* **2001**, *123*, 3268.

(10) Lawrence, J. D.; Li, H.; Rauchfuss, T. B. Beyond Fe-only hydrogenases: N-functionalized 2-aza-1,3-dithiolates $Fe_2[(SCH_2)_2NR](CO)_x$ (x = 5,6). *Chem. Commun.* **2001**, 1482.

(11) Czech, I.; Stripp, S.; Sanganas, O.; Leidel, N.; Happe, T.; Haumann, M. The [FeFe]-hydrogenase maturation protein HydF contains a H-cluster like [4Fe4S]-2Fe site. *FEBS Lett.* **2011**, *585*, 225.

(12) de Hatten, X.; Bothe, E.; Merz, K.; Huc, I.; Metzler-Nolte, N. A Ferrocene—Peptide Conjugate as a Hydrogenase Model System. *Eur. J. Inorg. Chem.* **2008**, *2008*, 4530.

(13) Durgaprasad, G.; Bolligarla, R.; Das, S. K. Synthesis, structural characterization and electrochemical studies of $[Fe_2(\mu-L)(CO)_6]$ and $[Fe_2(\mu-L)(CO)_5(PPh_3)]$ (L = pyrazine-2,3-dithiolate, quinoxaline-2,3-dithiolate and pyrido[2,3-b]pyrazine-2,3-dithiolate): Towards modeling the active site of [FeFe]-Hydrogenase. *J. Organomet. Chem.* **2011**, *696*, 3097.

(14) Erdem, Ö. F.; Schwartz, L.; Stein, M.; Silakov, A.; Kaur-Ghumaan, S.; Huang, P.; Ott, S.; Reijerse, E. J.; Lubitz, W. A Model of the [FeFe] Hydrogenase Active Site with a Biologically Relevant Azadithiolate Bridge: A Spectroscopic and Theoretical Investigation. *Angew. Chem., Int. Ed.* **2011**, *50*, 1439.

(15) Gao, W.; Song, L.-C.; Yin, B.-S.; Zan, H.-N.; Wang, D.-F.; Song, H.-B. Synthesis and Characterization of Single, Double, and Triple Butterfly [2Fe2E] (E = Se, S) Cluster Complexes Related to the Active Site of [FeFe]-Hydrogenases. *Organometallics* **2011**, *30*, 4097.

(16) Green, K. N.; Hess, J. L.; Thomas, C. M.; Darensbourg, M. Y. Resin-bound models of the [FeFe]-hydrogenase enzyme active site and studies of their reactivity. *Dalton Trans.* **2009**, 4344.

(17) Keita, B.; Floquet, S.; Lemonnier, J.-F.; Cadot, E.; Kachmar, A.; Benard, M.; Rohmer, M.-M.; Nadjo, L. A New Class of Efficient Electrocatalysts for the Reduction of Protons into Hydrogen Based on the $[Mo_2O_2S_2]^{2+}$ Building Block. *J. Phys. Chem. C* **2008**, *112*, 1109.

(18) Li, B.; Liu, T.; Popescu, C. V.; Bilko, A.; Darensbourg, M. Y. Synthesis and Mössbauer Characterization of Octahedral Iron(II) Carbonyl Complexes $FeI_2(CO)_3L$ and $FeI_2(CO)_2L_2$: Developing Models of the [Fe]-H_2ase Active Site. *Inorg. Chem.* **2009**, *48*, 11283.

(19) Li, P.; Wang, M.; Chen, L.; Liu, J.; Zhao, Z.; Sun, L. Structures, protonation, and electrochemical properties of diiron dithiolate complexes containing pyridyl-phosphine ligands. *Dalton Trans.* **2009**, 1919.

(20) Schwartz, L.; Eilers, G.; Eriksson, L.; Gogoll, A.; Lomoth, R.; Ott, S. Iron hydrogenase active site mimic holding a proton and a hydride. *Chem. Commun.* **2006**, 520.

(21) Singh, P. S.; Rudbeck, H. C.; Huang, P.; Ezzaher, S.; Eriksson, L.; Stein, M.; Ott, S.; Lomoth, R. (I,0) Mixed-Valence State of a Diiron Complex with Pertinence to the [FeFe]-Hydrogenase Active Site: An IR, EPR, and Computational Study. *Inorg. Chem.* **2009**, *48*, 10883.

(22) Song, L.-C.; Xie, Z.-J.; Liu, X.-F.; Ming, J.-B.; Ge, J.-H.; Zhang, X.-G.; Yan, T.-Y.; Gao, P. Synthetic and structural studies on new diiron azadithiolate (ADT)-type model compounds for active site of [FeFe]hydrogenases. *Dalton Trans.* **2011**, *40*, 837.

(23) Sun, L.; Åkermark, B.; Ott, S. Iron hydrogenase active site mimics in supramolecular systems aiming for light-driven hydrogen production. *Coord. Chem. Rev.* **2005**, *249*, 1653.

(24) Wang, H.-Y.; Wang, W.-G.; Si, G.; Wang, F.; Tung, C.-H.; Wu, L.-Z. Photocatalytic Hydrogen Evolution from Rhenium(I) Complexes to [FeFe] Hydrogenase Mimics in Aqueous SDS Micellar Systems: A Biomimetic Pathway. *Langmuir* **2010**, *26*, 9766.

(25) Zhan, C.; Wang, X.; Wei, Z.; Evans, D. J.; Ru, X.; Zeng, X.; Liu, X. Synthesis and characterisation of polymeric materials consisting of $\{Fe_2(CO)_5\}$-unit and their relevance to the diiron sub-unit of [FeFe]-hydrogenase. *Dalton Trans.* **2010**, *39*, 11255.

(26) Zhang, Y.; Hu, M.-Q.; Wen, H.-M.; Si, Y.-T.; Ma, C.-B.; Chen, C.-N.; Liu, Q.-T. Terminal pyridine-N ligation at [FeFe] hydrogenase active-site mimic. *J. Organomet. Chem.* **2009**, *694*, 2576.

(27) Harb, M. K.; Niksch, T.; Windhager, J.; Görls, H.; Holze, R.; Lockett, L. T.; Okumura, N.; Evans, D. H.; Glass, R. S.; Lichtenberger, D. L.; et al. Synthesis and Characterization of Diiron Diselenolato

Complexes Including Iron Hydrogenase Models. *Organometallics* **2009**, *28*, 1039.

(28) Wolpher, H.; Borgstrom, M.; Hammarstrom, L.; Bergquist, J.; Sundstrom, V.; Styring, S.; Sun, L.; Akermark, B. Synthesis and properties of an iron hydrogenase active site model linked to a ruthenium tris-bipyridine photosensitizer. *Inorg. Chem. Commun.* **2003**, *6*, 989.

(29) Ott, S.; Borgstrom, M.; Kritikos, M.; Lomoth, R.; Bergquist, J.; Åkermark, B.; Hammarstrom, L.; Sun, L. Model of the Iron Hydrogenase Active Site Covalently Linked to a Ruthenium Photosensitizer: Synthesis and Photophysical Properties. *Inorg. Chem.* **2004**, *43*, 4683.

(30) Song, L. C.; Tang, M. Y.; Mei, S. Z.; Huang, J. H.; Hu, Q. M. The Active Site Model for Iron-Only Hydrogenases Coordinatively Bonded to a Metalloporphyrin Photosensitizer. *Organometallics* **2007**, *26*, 1575.

(31) Kaziannis, S.; Santabarbara, S.; Wright, J. A.; Greetham, G. M.; Towrie, M.; Parker, A. W.; Pickett, C. J.; Hunt, N. T. Femtosecond to Microsecond Photochemistry of a [FeFe]hydrogenase Enzyme Model Compound. *J. Phys. Chem. B* **2010**, *114*, 15370.

(32) Ridley, A. R.; Stewart, A. I.; Adamczyk, K.; Ghosh, H. N.; Kerkeni, B. n.; Guo, Z. X.; Nibbering, E. T. J.; Pickett, C. J.; Hunt, N. T. Multiple-Timescale Photoreactivity of a Model Compound Related to the Active Site of [FeFe]-Hydrogenase. *Inorg. Chem.* **2008**, *47*, 7453.

(33) Bingaman, J. L.; Kohnhorst, C. L.; Van Meter, G. A.; McElroy, B. A.; Rakowski, E. A.; Caplins, B. W.; Gutowski, T. A.; Stromberg, C. J.; Webster, C. E.; Heilweil, E. J. Time-Resolved Vibrational Spectroscopy of [FeFe]-Hydrogenase Model Compounds. *J. Phys. Chem. A* **2012**, *116*, 7261.

(34) Schmidt, M.; Contakes, S. M.; Rauchfuss, T. B. First Generation Analogues of the Binuclear Site in the Fe-Only Hydrogenases: $Fe_2(\mu\text{-}SR)_2(CO)_4(CN)_{2}2$. *J. Am. Chem. Soc.* **1999**, *121*, 9736.

(35) Haines, R. J.; de Beer, J. A.; Greatrex, R. Reactions of metal carbonyl derivatives. Part XIX. Halogenation studies of di-[small micro]-alkylthio- and di-[small micro]-arylthio-bis(tricarbonyliron) and their substituted derivatives. *J. Chem. Soc., Dalton Trans.* **1976**, 1749.

(36) Tye, J. W.; Darensbourg, M. Y.; Hall, M. B. De Novo Design of Synthetic Di-Iron(I) Complexes as Structural Models of the Reduced Form of Iron-Iron Hydrogenase. *Inorg. Chem.* **2006**, *45*, 1552.

(37) Darensbourg, M. Y.; Lyon, E. J.; Zhao, X.; Georgakaki, I. P. The organometallic active site of [Fe]hydrogenase: Models and entatic states. *Proc. Natl. Acad. Sci. U. S. A.* **2003**, *100*, 3683.

(38) Zhao, X.; Georgakaki, I. P.; Miller, M. L.; Yarbrough, J. C.; Darensbourg, M. Y. H/D Exchange Reactions in Dinuclear Iron Thiolates as Activity Assay Models of Fe-H_2ase. *J. Am. Chem. Soc.* **2001**, *123*, 9710.

(39) Kania, R.; Frederix, P. W. J. M.; Wright, J. A.; Ulijn, R. V.; Pickett, C. J.; Hunt, N. T. Solution-phase photochemistry of a [FeFe]hydrogenase model compound: Evidence of photoinduced isomerisation. *J. Chem. Phys.* **2012**, *136*, 044521.

(40) Silaghi-Dumitrescu, I.; Bitterwolf, T. E.; King, R. B. Butterfly Diradical Intermediates in Photochemical Reactions of $Fe_2(CO)_6(\mu\text{-}S2)$. *J. Am. Chem. Soc.* **2006**, *128*, 5342.

(41) Certain commercial equipment, instruments, or materials are identified in this paper to adequately specify the experimental procedure. In no case does identification imply recommendation or endorsement by NIST.

(42) Dougherty, T. P.; Grubbs, W. T.; Heilweil, E. J. Photochemistry of $Rh(CO)_2$(acetylacetonate) and Related Metal Dicarbonyls Studied by Ultrafast Infrared Spectroscopy. *J. Phys. Chem.* **1994**, *98*, 9396.

(43) Frisch, M. J.; Trucks, G. W.; Schlegel, H. B.; Scuseria, G. E.; Robb, M. A.; Cheeseman, J. R.; Montgomery, J., J. A.; Vreven, T.; Kudin, K. N.; Burant, J. C. et al. Gaussian 03, Revision E.01; Gaussian, Inc.: Wallingford, CT, 2004.

(44) Becke, A. D. Density-functional exchange-energy approximation with correct asymptotic behavior. *Phys. Rev. A* **1988**, *38*, 3098.

(45) Perdew, J. P. Density-functional approximation for the correlation energy of the inhomogeneous electron gas. *Phys. Rev. B* **1986**, *33*, 8822.

(46) Perdew, J. P. Erratum: Density-functional approximation for the correlation energy of the inhomogeneous electron gas. *Phys. Rev. B* **1986**, *34*, 7406.

(47) Parr, R. G.; Yang, W. *Density-Functional Theory of Atoms and Molecules*; Oxford University Press: New York, 1989.

(48) Schafer, A.; Horn, H.; Ahlrichs, R. Fully optimized contracted Gaussian basis sets for atoms Li to Kr. *J. Chem. Phys.* **1992**, *97*, 2571.

(49) Schafer, A.; Huber, C.; Ahlrichs, R. Fully optimized contracted Gaussian basis sets of triple zeta valence quality for atoms Li to Kr. *J. Chem. Phys.* **1994**, *100*, 5829.

(50) Lyon, E. J.; Georgakaki, I. P.; Reibenspies, J. H.; Darensbourg, M. Y. Carbon Monoxide and Cyanide Ligands in a Classical Organometallic Complex Model for Fe-Only Hydrogenase. *Angew. Chem., Int. Ed.* **1999**, *38*, 3178.

(51) Frisch, M. J.; Trucks, G. W.; Schlegel, H. B.; Scuseria, G. E.; Robb, M. A.; Cheeseman, J. R.; Scalmani, G.; Barone, V.; Mennucci, B.; Petersson, G. A. et al. Gaussian 09, Revision A.02; Gaussian Inc.: Wallingford, CT, 2009.

(52) Perdew, J. P.; Zunger, A. Self-interaction correction to density-functional approximations for many-electron systems. *Phys. Rev. B* **1981**, *23*, 5048.

(53) Vosko, S. H.; Wilk, L.; Nusair, M. Accurate spin-dependent electron liquid correlation energies for local spin density calculations: a critical analysis. *Can. J. Phys.* **1980**, *58*, 1200.

(54) Hay, P. J.; Wadt, W. R. Ab initio effective core potentials for molecular calculations. Potentials for K to Au including the outermost core orbitals. *J. Chem. Phys.* **1985**, *82*, 299.

(55) Couty, M.; Hall, M. B. Basis sets for transition metals: Optimized outer p functions. *J. Comput. Chem.* **1996**, *17*, 1359.

(56) Hariharan, P. C.; Pople, J. A. The influence of polarization functions on molecular orbital hydrogenation energies. *Theor. Chim. Acta* **1973**, *28*, 213.

(57) Hehre, W. J.; Ditchfield, R.; Pople, J. A. Self-Consistent Molecular Orbital Methods. XII. Further Extensions of Gaussian-Type Basis Sets for Use in Molecular Orbital Studies of Organic Molecules. *J. Chem. Phys.* **1972**, *56*, 2257.

(58) The 6-31G(d′) basis set has the exponent for the d polarization function taken from the 6-311G(d) basis sets for C, O, and N atoms, instead of the value of 0.8 arbitrarily assigned in the 6-31G(d) basis sets.

(59) Dunlap, B. I. Fitting the Coulomb potential variationally in X alpha molecular calculations. *J. Chem. Phys.* **1983**, *78*, 3140.

(60) Dunlap, B. I. Robust and variational fitting: Removing the four-center integrals from center stage in quantum chemistry. *J. Mol. Struct.: THEOCHEM* **2000**, *529*, 37.

(61) Dunlap, B. I.; Connolly, J. W. D.; Sabin, J. R. On some approximations in applications of X alpha theory. *J. Chem. Phys.* **1979**, *71*, 3396.

(62) Dunlap, B. I.; Connolly, J. W. D.; Sabin, J. R. On first-row diatomic molecules and local density models. *J. Chem. Phys.* **1979**, *71*, 4993.

(63) Marques, M. A. L.; Gross, E. K. U. Time-Dependent Density Functional Theory. *Annu. Rev. Phys. Chem.* **2004**, *55*, 427.

(64) Furche, F.; Ahlrichs, R. Adiabatic time-dependent density functional methods for excited state properties. *J. Chem. Phys.* **2002**, *117*, 7433.

(65) Furche, F.; Ahlrichs, R. Erratum: Time-dependent density functional methods for excited state properties [*J. Chem. Phys.* [117], 7433 (2002)]. *J. Chem. Phys.* **2004**, *121*, 12772.

(66) Numerical frequency calculations revealed that all geometry-optimized excited state species, with the exception of **1-1***, each had one spurious imaginary frequency. See Supporting Information for further details.

(67) The error message provided in the output of each job was similar; "Fatal Problem: The smallest alpha delta epsilon is X, where X

corresponded to a value between $-0.97324308 \times 10^{-03}$ to $0.93356175 \times 10^{-03}$".

(68) Addison, A. W.; Rao, T. N.; Reedijk, J.; van Rijn, J.; Verschoor, G. C. Synthesis, structure, and spectroscopic properties of copper(II) compounds containing nitrogen-sulphur donor ligands; the crystal and molecular structure of aqua[1,7-bis(N-methylbenzimidazol-2[prime or minute]-yl)-2,6-dithiaheptane]copper(II) perchlorate. *J. Chem. Soc., Dalton Trans.* **1984**, *0*, 1349.